CAMES, **28**(3): 193–223, 2021, doi: 10.24423/cames.363

Prediction of Random Vibration Fatigue Damage Using Isogeometric Modelling

Shubiao WANG*, Leila KHALIJ, Renata TROIAN, Lujie SHI

Laboratory of Mechanics of Normandy (LMN)
Normandie Université, INSA Rouen Normandie
Rouen 76800, France
*Corresponding Author e-mail: shubiao.wang@insa-rouen.fr

The finite element analysis (FEA) method is indispensable in simulation technology, as it can help engineers predict results to avoid the cost of experimental testing. However, the finite element mesh generation process can be time-consuming, and the approximate mesh model can lead to inaccurate stress results. Improving the accuracy of stress estimation leads to a better assessment of damage or life of mechanical components. In this study, we applied the isogeometric analysis (IGA) implemented in LS-DYNA software to study two specimens subjreted to the stationary Gaussian random loads. These geometric models were represented by non-uniform rational B-spline (NURBS) to assess the damage and fatigue life in the frequency domain by using Dirlik's distribution and cumulative damage. A comparison with FEA was conducted to highlight the main differences. Experimental fatigue tests with an electrodynamic shaker were also carried out to check if the fatigue lives predicted by numerical models are consistent. The study showed that IGA predicts similar results to FEA with an acceptable relative error and reduced the time for mesh generation, requiring fewer integration points and mesh elements.

Keywords: isogeometric analysis, finite element method, random acceleration, vibration-based bending fatigue.

Notation

CPU – central processing unit,
FEA – finite element analysis,
HCF – high-cycle fatigue,
IGA – isogeometric analysis,
NURBS – non-uniform rational B-spline,
PSD – power spectral density,
RFD – resonant frequency deviation [%],
RMS – root mean square,
S-N – diagram that relates the stress amplitude to the number of cycles to failure,

e, cp – element and control point,
f – frequency [Hz],
$\sqrt{m_0}$ – root mean square value of stress,
m_k – k-th order spectral moment,
n^e – number of element,
n^e_{cp} – number of control points in an element e,
n, m – number of basis functions along ξ and λ parametric directions,
p, q – polynomial order along ξ and λ parametric directions,
D – total damage for deterministic loading,
$\mathrm{E}[D]$ – total damage for random loading,
$\mathrm{E}[N_0^+]$ – expected number of zero-crossing per unit time,
$\mathrm{E}[T_f]$ – fatigue life for random loading [s],
$F_\sigma(r)$ – cumulative density function of stress,
$L_{i,p}(\xi)$ – Lagrangian basis functions for FEA,
N – applied cycle number,
N_f – number of cycles allowable at a particular stress amplitude,
$N_{i,p}(\xi)$, $M_{j,q}(\lambda)$ – i-th and j-th B-spline basis functions of orders p and q defined at ξ and λ parametric points,
$R_{i,p}(\xi)$ – i-th NURBS basis functions of order p defined at ξ parametric point,
$R^{p,q}_{i,j}(\xi,\lambda)$ – i-th and j-th NURBS basis functions of orders p and q defined at ξ and λ parametric points,
$S_{\sigma\sigma}(f)$ – stress PSD function,
$p_\sigma(r)$ – probability density function of stress,
T – time duration [s],
$W(\xi)$ – weighted linear combination of B-spline basis functions,
σ_a – stress amplitude,
σ_f, b, C, β – deterministic Basquin's material constants,
$\sigma(t)$ – stress random process,
$\mathbf{e} = (e_1, e_2, e_3)^T$ – orthonormal basis,
$\mathbf{f}$ – deterministic volume force,
$\mathbf{n}$ – outward normal vector,
$\mathbf{t}$ – deterministic surface force,
$\mathbf{u}$, $\mathbf{u}^e$ – global and element displacement vector,
$\dot{\mathbf{u}}$, $\ddot{\mathbf{u}}$ – velocity and acceleration vectors,
$\mathbf{x} = (x, y, z)^T$ – global Cartesian reference system,
$\mathbf{B}$ – strain displacement matrix,
$\mathbf{C}$ – damping matrix,
$\mathbb{C}$ – fourth-order material constitutive tensor,
$\mathbf{F}$, $\mathbf{F}^e$ – global and element external force vector,
$|\mathbf{H}(f)|$ – magnitude of the frequency response matrix,
$\mathbf{K}$, $\mathbf{K}^e$ – global and element stiffness matrix,
$\mathbf{P}_i$ – i-th control point vector,
$\mathbf{R}$ – NURBS basis functions matrix,
$\mathbf{S}_{\mathrm{FF}}(f)$ – external force PSD matrix,
$\mathbf{S}_{\mathrm{uu}}(f)$ – displacement PSD matrix,
$\mathbf{S}_{\sigma\sigma}(f)$ – stress PSD matrix,

$\boldsymbol{\varepsilon}$ – strain tensor,
$\boldsymbol{\eta}$ – parametric coordinates given by ξ in one dimension, (ξ, λ) in 2 dimensions and (ξ, λ, ζ) in 3 dimensions,
$\boldsymbol{\sigma}$ – Cauchy stress tensor,
$\boldsymbol{\Xi}$, $\boldsymbol{\Lambda}$ – knot vectors,
E[.] – expected value operator,
δ – used for virtual quantities,
∇ – divergence operator,
$\otimes$ – tensor product.

1. Introduction

Based on industrial data, 80% to 95% of mechanical structures fail due to fatigue [1]. Predicting fatigue strength is essential in identifying the effective life before a design is used in the natural working environment. In most cases, the fatigue loads are random, and the most appropriate approach is to use a probabilistic method to develop fatigue analysis. Fatigue analysis can be conducted in the time or frequency domain for Gaussian random processes. However, time-domain analysis is more computationally expensive compared to the method using a power spectral density (PSD) in the frequency domain. Dirlik's model [1, 2] was used in this work to calculate the expected fatigue damage from spectral moments of the PSD.

Numerical modelling of a complex structure is another time-consuming aspect. Nowadays, mechanical systems are an assembly of many components, leading to specific requirements on numerical analysis methods in terms of accuracy and speed of analysis. A conventional finite element analysis (FEA) has some weaknesses. The time spent for mesh generation process is often much longer than the analysis time [3]. It is estimated that 80% of analysis time is devoted to the mesh generation in some fields, e.g., automotive or shipbuilding industries [4]. On the other hand, it is often necessary to communicate with the original geometry during each mesh refinement, and this process is time-consuming.

The second disadvantage lies in geometric approximation. Indeed, it is challenging to accurately represent complex geometric models based on the Lagrangian basis function in the classical FEA. Thus, the approximate models lead to inaccurate analysis results. A possible alternative to finite elements is the isogeometric analysis (IGA), often based on non-uniform rational B-splines (NURBS) basis functions. In this case, a geometric model can be described exactly by NURBS mesh elements. The corresponding mesh generation and mesh refinement processes are often time-saving.

Hughes *et al.* [4] first proposed the concept of IGA. At present, IGA is applied in many fields, including contact mechanics [5–7], fluid mechanics [8–10], structural optimization [11–14], shell analysis [15–19], damage and fracture me-

chanics [20, 21], structural vibration analysis [22–26], and vibration analysis with random material properties in which Young's modulus and mass density are modelled as Gaussian random variables [26]. Kiendl *et al.* [19] introduced an isogeometric bending analysis of a thin shell structure comprised of multiple patches. Gondegaon and Voruganti [25] presented a MATLAB code for different types of structures with static and vibration analysis. Hartmann *et al.* [27] presented an isogeometric convergence analysis of an underbody cross member under the condition of increasing polynomial orders and element size. Comparison with the FEA results has shown that IGA with higher polynomial order sometimes does not give better results if the change in control point spacing is not significant. Under the condition of comparable discretization with standard linear finite elements, the NURBS shell elements can produce good results as those produced by FEA with less central processing unit (CPU) time.

In the literature, numerous studies have been focused on modal and vibration modelling. However, to the authors' knowledge, no research on random vibration fatigue analysis with IGA has been reported. This work presents the NURBS-based IGA applied to a structure subjected to random vibration fatigue load. The analysis results have been verified by the classical FEA, in which LS-DYNA software was used for the numerical analysis. The present work contributes to improving the development of random vibration in LS-DYNA [28]. Furthermore, to validate the fatigue life results, experimental tests with an electrodynamic shaker are carried out.

This paper is organized as follows. Section 2 briefly reviews the basic concepts of IGA, formulations, and the differences between IGA and FEA. Then the isogeometric static analysis of a plate with a hole model is conducted, and FEA and analytical solution validate the analysis results. Section 3 presents the isogeometric random vibration fatigue analysis of a plate with a notch model, and the FEA and experimental test confirm the results. Conclusions are proposed in Sec. 4.

2. Theoretical background

A comparison of IGA with FEA is given to set the study's theoretical framework, which focuses on the application of the isogeometric analysis of a structure subjected to fatigue induced by random vibration. Static calculations are also considered to study the discretized model convergence.

2.1. Basic concepts of isogeometric analysis

IGA used in this research is based on NURBS basis functions. NURBS can exactly represent a complex geometry, such as the conical, sphere, and cylindrical

shapes. More details can be found in [4]. The basis functions are completely determined by the knot-vector and the polynomial degree. As the concept of IGA is relatively well known in the academic computing community, only the basics are given next.

2.1.1. Parameter space and patch. The parameter space in a two-dimensional IGA (R and S dimensions) is the $[0,1] \times [0,1]$ space where the NURBS basis functions are defined. The patch is called a subdomain in IGA (can be seen as a macro element), in which we can define the material properties and section characteristics. A patch consists of numerous mesh elements. A geometric model can be represented by several patches in which we can set different material properties or section details, such as thickness. We use one patch model for the first application (plate with a hole) for this study.

2.1.2. Knot vector. A knot vector is defined as a series of non-decreasing coordinates in parameter space, denoted by $\boldsymbol{\Xi} = \{\xi_1, \xi_2, ..., \xi_{n+p+1}\}$, where $\xi_i \in \mathbb{R}$ is the i-th knot (coordinate), $i = 1, 2, ..., n+p+1$ is the knot index, and n and p are the number and the polynomial order of B-spline basis functions, respectively.

We use the 2D shell elements for this study, so the discretization is conducted in two dimensions, R and S, with two corresponding knot vectors. Each knot or coordinate of the knot vector is used to divide the parameter space of a geometric model to obtain elements, and the boundary of isogeometric mesh elements in physical space is simply the image of the knot line under B-spline mapping. This means that we can select the certain mesh elements by the corresponding knot vectors.

2.1.3. B-splines. B-splines are defined by piecewise polynomials of a degree p. They are completely defined by the knots such as $\xi_1 \leq \xi_2 \leq ... \leq \xi_{n+p+1}$. More specifically, the B-splines are defined by Eqs (1) and (2).

For $i = 1, ..., n$ $(p = 0)$, the B-splines are constructed with:

$$N_{i,0}(\xi) = \begin{cases} 1 & \text{if} \quad \xi \in \lceil \xi_i, \xi_{i+1} \rceil, \\ 0 & \text{otherwise.} \end{cases} \tag{1}$$

To generate B-splines of arbitrary order $p > 0$, the following equation can be used:

$$N_{i,p}(\xi) = \frac{\xi - \xi_i}{\xi_{i+p} - \xi_i} N_{i,p-1}(\xi) + \frac{\xi_{i+p+1} - \xi}{\xi_{i+p+1} - \xi_{i+1}} N_{i+1,p-1}(\xi). \tag{2}$$

Thus, a B-spline curve is defined by the linear combination of B-spline basis functions with the corresponding control points $\mathbf{P}_i$ in physical space ($i = 1, ..., n$) as coefficients:

$$\mathbf{c}(\xi) = \sum_{i=1}^{n} N_{i,p}(\xi)\mathbf{P}_i. \tag{3}$$

2.1.4. Non-uniform rational B-splines. To generate circular shapes, NURBS is introduced. The univariate NURBS basis function is described by the rationale of weighted B-spline basis functions:

$$R_{i,p}(\xi) = \frac{\omega_i N_{i,p}(\xi)}{W(\xi)} = \frac{\omega_i N_{i,p}(\xi)}{\sum\limits_{j=1}^{n} \omega_j N_{j,p}(\xi)}. \tag{4}$$

Here, n denotes the number of NURBS basis functions along ξ direction. $\omega_i \in \mathbb{R}$ denotes the weight value of the control point $\mathbf{P}_i$, and $W(\xi)$ is the weighted linear combination of B-spline basis functions. The NURBS curve is defined by the linear combination of univariate NURBS basis functions $R_{i,p}(\xi)$ and control points $\mathbf{P}_i$ by the following expression [4]:

$$\mathbf{c}(\xi) = \sum_{i=1}^{n} R_{i,p}(\xi)\mathbf{P}_i. \tag{5}$$

Given two knot vectors (one for each parametric direction) $\boldsymbol{\Xi} = \{\xi_1, \xi_2, ..., \xi_{n+p+1}\}$ and $\boldsymbol{\Lambda} = \{\lambda_1, \lambda_2, ..., \lambda_{n+p+1}\}$, the NURBS surface is defined by:

$$\mathbf{s}(\xi, \lambda) = \sum_{i=1}^{n}\sum_{j=1}^{m} R_{i,j}^{p,q}(\xi, \lambda)\mathbf{P}_{i,j}, \tag{6}$$

where $R_{i,j}^{p,q}(\xi, \lambda)$ is bivariate NURBS basis functions defined by:

$$R_{i,j}^{p,q}(\xi, \lambda) = \frac{N_{i,p}(\xi)M_{j,q}(\lambda)w_{i,j}}{\sum\limits_{k=1}^{n}\sum\limits_{l=1}^{m} N_{k,p}(\xi)M_{l,q}(\lambda)w_{k,l}}, \tag{7}$$

where $N_{i,p}(\xi)$ and $M_{j,q}(\lambda)$ are p-th and q-th order B-spline basis functions.

2.2. Formulations

Let us consider a body and the global Cartesian reference system $\mathbf{x} = (x, y, z)^T$ and its associated orthonormal basis $\mathbf{e} = (e_1, e_2, e_3)^T$. The body is

subjected to the volume forces $\mathbf{f} = \mathrm{f}_i \mathbf{e}_i$ and traction vector acting on the body surface $\mathbf{t} = t_i \mathbf{e}_i$. The domain of the body $\boldsymbol{\Omega}$ is bounded by prescribed displacement Γ_u and traction Γ_t boundaries. We can introduce the displacement field as $\mathbf{u} = u_i \mathbf{e}_i$ and the stress $\boldsymbol{\sigma} = \sigma_{ij} \mathbf{e}_i \otimes \mathbf{e}_j$ $(i, j = 1, ..., 3)$ satisfying the equation in the strong form:

$$\nabla \boldsymbol{\sigma} + \mathbf{f} = \rho \frac{\partial^2 \mathbf{u}}{\partial t^2} \quad \text{in } \Omega, \tag{8}$$

$$\boldsymbol{\sigma} \cdot \mathbf{n} = \mathbf{t} \quad \text{in } \Gamma_t, \tag{9}$$

where ∇ represents the divergence operator, ρ is the density assumed constant, $\mathbf{n}$ is the outward normal vector, and $\frac{\partial^2 \mathbf{u}}{\partial t^2} = \ddot{\mathbf{u}}$ is the acceleration vector of the body. This term stands for the inertial effect, which is considered negligible for a static problem.

The displacement field is approximated using NURBS basis functions to construct the CAD geometry of the structure. The discretization of the domain $\boldsymbol{\Omega}$ into a number of sub-domains $\boldsymbol{\Omega}^e = [\xi_i, \xi_{i+1}] \otimes [\lambda_j, \lambda_{j+1}]$ is carried out by using the B-spline and NURBS formulations described in Subsec. 2.1, which transform the parametric coordinates to physical coordinates. A mapping is introduced to perform the analysis of each control point cp of any element e:

$$\mathbf{x}^e(\boldsymbol{\eta}) = \sum_{cp=1}^{n_{cp}^e} R_{cp}^e(\boldsymbol{\eta}) \mathbf{P}_{cp}^e, \tag{10}$$

where $\boldsymbol{\eta}$ contains the parametric coordinates given by ξ in one dimension and (ξ, λ) in two dimensions, and n_{cp}^e is the number of control points over element e. Using the Galerkin method, the displacement and virtual displacement fields can be deduced as follows:

$$\mathbf{u}^e(\mathbf{x}) = \sum_{cp=1}^{n_{cp}^e} R_{cp}^e(\boldsymbol{\eta}) \mathbf{u}_{cp}^e, \tag{11}$$

$$\delta \mathbf{u}^e(\mathbf{x}) = \sum_{cp=1}^{n_{cp}^e} R_{cp}^e(\boldsymbol{\eta}) \delta \mathbf{u}_{cp}^e, \tag{12}$$

where $\mathbf{u}_{cp}$ and $\delta \mathbf{u}_{cp}$ correspond to the values of the displacement and virtual displacement fields at the control point $\mathbf{P}_{cp}$. The momentum equation of Eq. (8) can be used in a weak form based on the virtual work principle which can be built for each element e to obtain the governing dynamic equilibrium of motion for a structure:

$$\mathbf{M}^e \, \ddot{\mathbf{u}}^e + \mathbf{C}^e \, \dot{\mathbf{u}}^e + \mathbf{K}^e \, \mathbf{u}^e = \mathbf{F}^e, \tag{13}$$

where $\mathbf{u}^e$ is the control point displacement, $\mathbf{F}^e$ is the external force vector that represents the contribution of the total body forces, and $\mathbf{M}^e$, $\mathbf{C}^e$ and $\mathbf{K}^e$ are the isogeometric element mass, damping using the damping property of an element e denoted by κ, and stiffness matrices, respectively, given by:

$$\mathbf{M}^e = \int_{\Omega} \rho\, \mathbf{R}^{eT}\, \mathbf{R}^e \mathrm{d}\Omega^e, \tag{14}$$

$$\mathbf{C}^e = \int_{\Omega} \kappa\, \mathbf{R}^{eT}\, \mathbf{R}^e \mathrm{d}\Omega^e, \tag{15}$$

$$\mathbf{K}^e = \int_{\Omega^e} \mathbf{B}^{eT}\, \mathbb{C}\, \mathbf{B}^e\, \mathrm{d}\Omega^e, \tag{16}$$

where $\mathbb{C} = \mathbb{C}_{ijkl}\mathbf{e}_i \otimes \mathbf{e}_j \otimes \mathbf{e}_k \otimes \mathbf{e}_l$ and $\boldsymbol{\varepsilon} = \varepsilon_{ij}\mathbf{e}_i \otimes \mathbf{e}_j$ are the fourth-order material elastic and the strain tensors, respectively. The components of strain tensor can also be formulated from displacement as follows:

$$\varepsilon_{ij} = \frac{1}{2}[u_{i,j} + u_{j,i}]. \tag{17}$$

$\mathbf{R}$ is the matrix of the NURBS basis function and $\mathbf{B}$ is the strain displacement matrix. It can be obtained by computing the derivatives of the basis functions $R_{cp}(\boldsymbol{\eta})$ for any element e. In bidimensional problem, the matrix has the following form:

$$\mathbf{B} = \begin{bmatrix} R_{1,x} & 0 & \dots & R_{i,x} & 0 & \dots & R_{n_{cp},x} & 0 \\ 0 & R_{1,y} & \dots & 0 & R_{i,y} & \dots & 0 & R_{n_{cp},y} \\ R_{1,y} & R_{1,x} & \dots & R_{i,y} & R_{i,x} & \dots & R_{n_{cp},y} & R_{n_{cp},x} \end{bmatrix}. \tag{18}$$

The global matrices can be assembled by their corresponding elemental matrices as follows:

$$\mathbf{M} = \sum_{e=1}^{n^e} \mathbf{M}^e, \quad \mathbf{C} = \sum_{e=1}^{n^e} \mathbf{C}^e, \quad \mathbf{K} = \sum_{e=1}^{n^e} \mathbf{K}^e, \quad \text{and} \quad \mathbf{F} = \sum_{e=1}^{n^e} \mathbf{F}^e. \tag{19}$$

The equations for 3D static calculations are given by Agrawal and Gautam [29].

2.3. Differences between IGA and FEA

The differences between IGA and FEA are the mesh elements formulation, choice of basis functions, and calculation of field variables in the governing equation. As shown in Fig. 1, the mesh model obtained in FEA consists of mesh

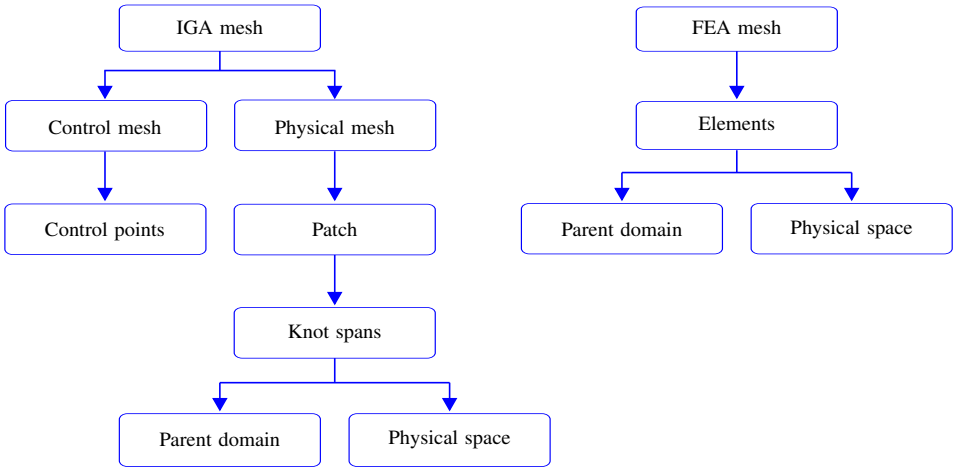

FIG. 1. Meshing process in isogeometric and finite element analysis.

elements represented in physical space or parent domain [30]. In physical space, the mesh elements are defined by their nodal coordinates, and finite element basis functions, i.e. Lagrangian functions [29], interpolating the coordinate between the nodes. Each element in the physical space can be mapped to the parent domain through coordinate transformation, in which the width and length of the parent element are respectively 1, and the Gauss integration is performed on the parent element.

In IGA besides the usual physical mesh and mesh in the parent domain, the control mesh is introduced. The control mesh is defined by control points. It defines geometry; however, it does not have to coincide with the real geometry of a studied object. In two dimensions the control mesh is a bilinear quadrilateral element [4]. The physical mesh is a representation of that actual geometry. It is obtained by the projection of control points with NURBS basis functions, and the discretization is governed by knot vectors discretization in the parent domain. A physical mesh model can consist of several patches, e.g., subdomains in which the section and material properties are the same.

Next, IGA usually adopts NURBS as its basis functions. Compared to Bernstein or B-spline basis functions, the NURBS basis functions possess more flexible properties and can exactly represent conic, circular and sphere models due to the effects of the B-spline basis function and weight points associations [29]. For FEA, the Lagrangian basis functions shown in Eq. (20) are used to approximate solutions at element nodes [30]:

$$L_{i,p}(\xi) = \prod_{k=1,k\neq i}^{p+1} \frac{\xi - \xi_k}{\xi_i - \xi_k}, \quad 1 \leq k \leq p+1 \quad \text{and} \quad -1 \leq \xi \leq 1. \tag{20}$$

Due to the different nature of basis functions, the description model also gives different results. The critical properties are in variation diminishing characteristics and inter-element boundary continuity. The variation diminishing property (the number of sign changes) is used to characterize the smoothness of a curve. For FEA, the Lagrangian basis functions can have any sign ($-1 \leq \xi \leq 1$, $-1 \leq L_{i,p}(\xi) \leq 1$), so the oscillation of the fitting curve would be increased with the increase in the polynomial order, resulting in a non-smooth representation of the fitting curve (which cannot satisfy the variation diminishing property) and leading to contact problems between different description models. In IGA, the NURBS basis functions can satisfy non-negativity ($-1 \leq \xi \leq 1$, $0 \leq R_{i,p}(\xi)$). The obtained results are less sensitive to the polynomial orders and can present a smooth representation of the geometry (possess the variation diminishing property) and the contact surfaces. The same is observed for the NURBS curves.

Additionally, the NURBS basis functions present c^{p-1-k} continuity, in which k is the number of repeating knots in a knot vector. However, the finite element basis functions are restricted to only c^0 continuity, leading to a non-smooth representation of the physical derivative quantities like stresses or strains.

Thirdly, in IGA, the combination of control points $\mathbf{P}_i$ and NURBS basis functions as shown in Eq. (4) are used to define NURBS-based elements, and the field variables, such as displacement $\mathbf{u}$ in Eq. (11), are performed on control points.

2.4. Comparison for a thin plate with a hole at the centre

The following well-known application [29, 31] is used to validate the isogeometric and finite element models developed in LS-DYNA software based on Kirsch's solution. A rectangular plate with a hole of radius a is loaded in the plane by a one-direction tension denoted by σ_∞. The plane stress condition is considered. The plate parameters are depicted in Fig. 2 and the related analytical solution of the stress around the hole is given by [32]:

$$\begin{aligned}
\sigma_{rr} &= \frac{\sigma_\infty}{2}\left(1-\left(\frac{a}{r}\right)^2\right)+\frac{\sigma_\infty}{2}\left(1-4\left(\frac{a}{r}\right)^2+3\left(\frac{a}{r}\right)^4\right)\cos 2\theta,\\
\sigma_{\theta\theta} &= \frac{\sigma_\infty}{2}\left(1+\left(\frac{a}{r}\right)^2\right)-\frac{\sigma_\infty}{2}\left(1+3\left(\frac{a}{r}\right)^4\right)\cos 2\theta,\\
\tau_{r\theta} &= -\frac{\sigma_\infty}{2}\left(1+2\left(\frac{a}{r}\right)^2\right)-3\left(\frac{a}{r}\right)^4\sin 2\theta.
\end{aligned} \tag{21}$$

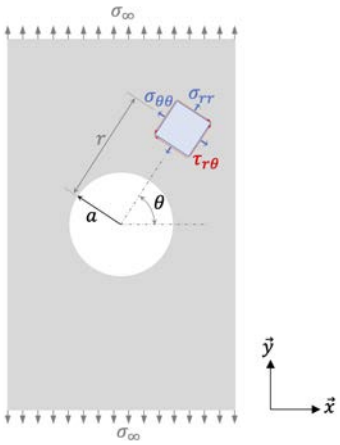

FIG. 2. Schematic diagram of a plate model.

At the hole ($r = a$), Eq. (21) becomes (the radial stress σ_{rr} and the shear stress $\tau_{r\theta}$ are zero):

$$\begin{aligned} &\sigma_{rr} = 0, \\ &\sigma_{\theta\theta} = \sigma_\infty(1 - 2\cos 2\theta), \\ &\tau_{r\theta} = 0. \end{aligned} \tag{22}$$

In addition, when $\theta = \pm 90^\circ$, the proportion between the obtained maximum stress $\sigma_{\theta\theta}$ and the applied stress σ_∞ is 3. This analytical solution is used in the following section to compare FEA and IGA.

2.4.1. Numerical models. The plate geometric model with $10 \times 2 \times 0.001$ (m) dimensions is modelled in LS-DYNA software. The radius of the hole is chosen at 0.25 m. The material properties of the model are given in Table 1. Due to the symmetry of the geometry and the applied load, just a quarter of the plate model is analyzed.

TABLE 1. Material properties of the plate.

Mass density	Young's modulus	Poisson's ratio
7800 kg/m^3	205 GPa	0.3

The related isogeometric and finite element mesh models, presented in Fig. 3, are defined with different densities of mesh elements to perform convergence analysis. Based on the obtained results, the CPU time for the analysis, and the maximum stress in the y-direction are respectively compared for IGA and FEA.

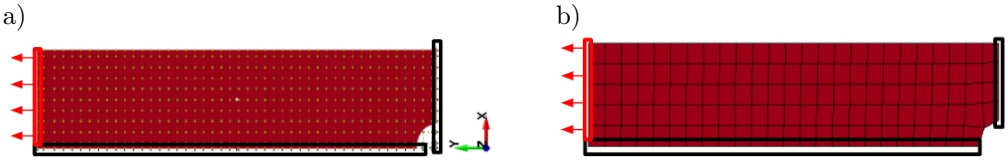

FIG. 3. Mesh models and boundary conditions: a) IGA, b) FEA.

The isogeometric shell elements with NURBS, specifically developed for IGA, are used for the model. The quadrilateral four-node elements are adopted to develop the FEA mesh model. The symmetry boundary conditions, depicted in Fig. 3, are the same for IGA and FEA. The translational displacements in the y-direction and x-direction, marked by black bracket, are respectively imposed on the bottom and right edges of the model. A tension load fixed at 1 MPa (marked by red a bracket) is applied onto the control points (for IGA) and nodes (for FEA) on the left edge of the model.

2.4.2. Convergence analysis. The maximum stress in the y-direction obtained from the static analysis is chosen to determine the convergence rate. In Fig. 4, it can be seen that with the increase of control points number of IGA and element nodes number of FEA, the maximum stresses tend to reach a stable value. In order to show the isogeometric convergence analysis intuitively, a fitting curve is used to approximate the obtained maximum stresses from different analyses. Furthermore, the minimum correlation coefficient r, defined by Eq. (23) between the maximum stress values and the values obtained from the fitting curve, is 0.92:

$$r = \frac{\sum_{i=1}^{n}(Y_i - \overline{Y})(Y_{fit,i} - \overline{Y}_{fit})}{\sqrt{\sum_{i=1}^{n}(Y_i - \overline{Y})^2}\sqrt{\sum_{i=1}^{n}(Y_{fit,i} - \overline{Y}_{fit})^2}}, \tag{23}$$

where Y_i and $Y_{fit,i}$ are the i-th values obtained from the numerical analysis and fitting curves, $\overline{Y}$ and $\overline{Y}_{fit}$ are corresponding mean values, and n is the extracted number sets and in this case n is 7.

For IGA, the maximum stress values start to converge from the mesh density (control point number for IGA) 933. For FEA, the maximum stresses become stable from the mesh density (element node number for FEA) 7701. After choosing the isogeometric and finite element convergence points, the analysis results of these points are obtained to compare IGA and FEA.

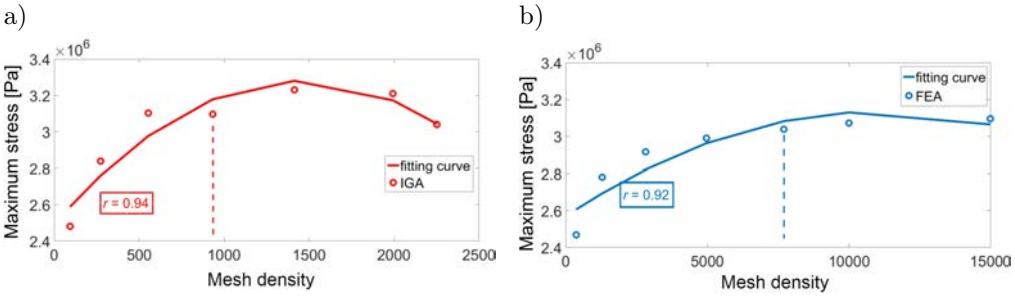

FIG. 4. Convergence analysis results: a) IGA, b) FEA.

2.4.3. Maximum stress in y-direction and CPU time. As the zone of maximum stresses is always located in similar elements, just a part of the model is shown in Fig. 5 in which the maximum stresses obtained from the isogeometric and finite element convergence analysis are respectively 3.098×10^6 and 3.015×10^6 Pa, leading to the relative error (defined by Eq. (24)) of 2.7%. Furthermore, it has been shown that maximum stress values are situated on the same elements. On the other hand by comparing CPU time, which shows the consumed time during the analysis process, we can find that IGA is more time-efficient compared to FEA, as the CPU time for IGA and FEA is respectively 74 s and 720 s.

All the numerical calculations presented in the article are run on the computer Intel(R) Core(TM) i5-6440HQ CPU 2.60GHz with RAM 8Gb.

$$\text{Relative error}(\%) = \frac{\text{Result}_{\text{IGA}} - \text{Result}_{\text{FEA}}}{\text{Result}_{\text{FEA}}}. \tag{24}$$

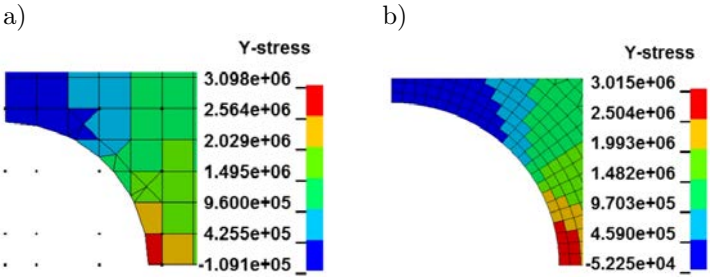

FIG. 5. Maximum stresses: a) IGA, b) FEA.

3. Fatigue analysis induced by random acceleration

The study of the dynamic response exploiting vibration phenomena aims to determine the dynamic properties directly connected with the geometrical

and mechanical characteristics of a system. Hence, some concepts of structural dynamic response and how to obtain the dynamic parameters are summarized in this section. The excitation with base motion (e.g., car suspension, earthquake ground motion or electrodynamic shaker, etc.) does not provide information with respect to the force applied. Therefore the formalism related to the base motion is different from the classical force-excitation theory.

For random vibration loading, the global matrices $\mathbf{M}$, $\mathbf{C}$ and $\mathbf{K}$ (and mode shapes) given in Eq. (13) remain deterministic. In the time domain, the force and the displacement field are written in terms of expected values denoted, respectively, as $\mathrm{E}[\mathbf{F}(t)]$ and $\mathrm{E}[\mathbf{u}(t)]$. In the spectral domain, these two quantities are connected by the following relation:

$$\mathbf{S}_{\mathrm{uu}}(f) = \left|\mathbf{H}_{\mathrm{uF}}(f)\right|^2 \mathbf{S}_{\mathrm{FF}}(f), \tag{25}$$

where $\mathbf{S}_{\mathrm{uu}}(f)$ and $\mathbf{S}_{\mathrm{FF}}(f)$ are the PSDs of control point displacement and external forces and $|\mathbf{H}_{\mathrm{uF}}(f)|$ corresponds to the frequency response magnitude of the structure obtained from the ratio between the displacement and the force given in the frequency domain. In the time domain, the stress expected value of the structure can therefore be deduced from the force expected value by using the following expression:

$$\mathrm{E}[\boldsymbol{\sigma}(t)] = \mathbb{C}\,\mathbf{B}\,\mathbf{K}^{-1}\,\mathrm{E}[\mathbf{F}(t)], \tag{26}$$

where $\mathbf{K}^{-1} = \mathbf{H}_{\mathrm{uF}}(0)$ represents the static part. The transformation of Eq. (26) into the spectral domain leads to a relationship between the stress and displacement PSDs:

$$\mathbf{S}_{\sigma\sigma}(f) = \mathbb{C}\,\mathbf{B}\,\mathbf{S}_{\mathrm{uu}}(f)\,\mathbf{B}^T\,\mathbb{C}^T. \tag{27}$$

In the following section, only one excitation direction is considered; therefore, matrices are not used.

3.1. Cumulative fatigue and frequency formulation for deterministic and random excitation

Fatigue is defined as a progressive change in the material properties following the application of loading cycles, the repetition of which can lead to the fracture. Schijve [33] defined fatigue life as the addition of the initiation period and the crack growth period. The author found that more than 90% of the fatigue life is usually spent before cracks under high cycle fatigue (HCF) conditions are detected. A cumulative damage calculation was used to quantify the total damage characterized by the fraction of life consumed by the crack initiation.

This study is focused on HCF; thus the material behavior remains elastic during the fatigue loading until crack initiation. Therefore, an elastic computation is performed to obtain stress states used for the damage calculations. For deterministic excitation, the linear model of Palmgren–Miner damage accumulation [34, 35] known as Miner's rule, is one of the most widely used methods [36–38]. Let us consider m stress amplitudes denoted by $\sigma_{a,i}$ $(i = 1, ..., m)$, which characterize the time history response calculated at the maximum stress location of a structure (by FEA or IGA). The authors assume that each significant stress amplitude extracted from the stress-time history (by using Rainflow counting techniques, see [39, 40]) produces individual damage and the total damage D is obtained by the following summation:

$$D = \sum_{i=1}^{m} \frac{1}{N_{f,i}} N_i, \tag{28}$$

where $N_{f,i}$ is the number of cycles allowable at particular stress before a material fails by fatigue (the number of cycles to failure at constant stress amplitude σ_a) defined from the S-N curve (representing the stress amplitudes versus the number of cycles to failure) and N_i is the ith applied stress cycle number. For steel structures, if the cumulative fatigue damage reaches a critical value of 1, the structure is considered damaged. To define the S-N relationship for high cycle fatigue region, the Basquin's power-law is used:

$$\sigma_a = \sigma_f N_f^b, \tag{29}$$

which can also be written as:

$$N_f \sigma_a^\beta = C \tag{30}$$

with $\sigma_f = C^{\frac{1}{\beta}}$ and $b = -\frac{1}{\beta}$.

Therefore, Eq. (28) becomes:

$$D = \sum_{i=1}^{m} C^{-1} \sigma_{a,i}^\beta N_i, \tag{31}$$

where C and β are material constants identified by the Basquin's straight curve in a logarithmic representation of the S-N curve.

For a deterministic loading, the fatigue analysis is performed in the time domain while for Gaussian random excitation, it can be developed in the time domain or the frequency domain. However, the fatigue analysis in the time domain requires a large number of time records compared to the frequency domain. Therefore, in this work, we consider only frequency formulations. When random

loading is considered, the damage and fatigue life are random variables. The random process $\sigma(t)$ corresponds to a random variation in time of a stress component or effective stress. At each instant, the process is composed of a number of random variables that follow a Gaussian distribution. All parameters useful for fatigue analysis performed in the frequency domain can be directly extracted from stress the PSD. When a Gaussian stationary random process is considered, these parameters are mainly the k-th order spectral moments given by:

$$m_k = \int_{-\infty}^{+\infty} |2\pi f|^k \, S_{\sigma\sigma}(f) \mathrm{d}f, \tag{32}$$

where $S_{\sigma\sigma}(f)$ is the stress PSD function. Over a duration of observation T, the probability that a random process $\sigma(t)$ does not exceed, in absolute value, a given value denoted by r can be given by the cumulative density function of the amplitudes (or maxima for zero-mean stress) denoted by $F_\sigma(r)$:

$$F_\sigma(r) = \int_{-\infty}^{r} p_\sigma(r) \mathrm{d}r = \mathrm{prob}(|\sigma(t)| \leq r), \quad t \in [0, T], \tag{33}$$

where $p_\sigma(r)$ is the probability density function. When the mechanical structure is subjected to a zero-mean Gaussian stationary random excitation, the expected damage per unit time can be obtained from the cumulative expression given in Eq. (28):

$$\mathrm{E}[D] = C^{-1} \mathrm{E}\left[|\sigma(t)|^\beta\right] \mathrm{E}[N], \tag{34}$$

where C and β are deterministic. To determine the expected value of $|\sigma(t)|^\beta$, we can use the expectation definition of a random variable in the HCF domain such as:

$$\mathrm{E}\left[|\sigma(t)|^\beta\right] = \int_0^{+\infty} r^\beta p_\sigma(r) \mathrm{d}r. \tag{35}$$

It corresponds to β-th order statistical moment. Knowing that for period T, $\mathrm{E}[N] = T \times \mathrm{E}[N_0^+]$, Eq. (34) becomes:

$$\mathrm{E}\left[D\right] = C^{-1} T \mathrm{E}[N_0^+] \int_0^{+\infty} r^\beta p_\sigma(r) \mathrm{d}r. \tag{36}$$

$\mathrm{E}[N_0^+] = \sqrt{\frac{m_2}{m_0}}$ is the expected number of zero-crossings with a positive slope per second. m_0 and m_2 are respectively the zeroth-order and second-order spectral moments of the PSD. $\sqrt{m_0}$ is the root mean square (RMS) and represents the square root of the area under the PSD-frequency graph. The expected fatigue life denoted by $\mathrm{E}[T_f]$ can then be deduced from Eq. (36):

$$\mathrm{E}[T_f] = \frac{T}{\mathrm{E}[D]} = \frac{1}{C^{-1}\mathrm{E}[N_0^+] \int\limits_0^{+\infty} r^\beta p_\sigma(r)\mathrm{d}r}. \tag{37}$$

Before the damage evaluation, it is necessary to define a probability density function $p_\sigma(r)$ of the maxima. The different spectral methods for fatigue damage assessment are first characterized by the cycle counting procedure. Since the rainflow method has been recognized to give the best predictions, the spectral methods are mainly focused on the rainflow cycle distribution. There is no analytical formula to establish the cycle distribution; therefore, the existing spectral methods evaluate these distributions approximately or empirically. Some of the most commonly used methods include the narrow-band approach based on Rayleigh approximation and Dirlik's amplitude distribution [2].

In this work, Dirlik's distribution is used to evaluate the expected value of damage from Eqs (36) and (37). The amplitude probability density function for a normalized variable $Z = \frac{\sigma_a}{\sqrt{m_0}}$ is:

$$p_\sigma(Z) = \frac{\frac{D_1}{Q} \cdot e^{\frac{-Z}{Q}} + \frac{D_2 \cdot Z}{R^2} \cdot e^{\frac{-Z^2}{2 \cdot R^2}} + D_3 Q \cdot e^{\frac{-Z^2}{2}}}{2\sqrt{m_0}}, \tag{38}$$

γ is the irregularity factor given by:

$$\gamma = \frac{m_2}{\sqrt{m_0 m_4}} \tag{39}$$

with m_4 the fourth-order spectral moment of the PSD. x_m is defined by Dirlik as the mean frequency and is expressed such as:

$$x_m = \frac{m_1}{m_0}\sqrt{\frac{m_2}{m_4}}, \tag{40}$$

and the other parameters are obtained from:

$$D_1 = \frac{2(x_m - \gamma^2)}{1+\gamma^2}, \qquad D_2 = \frac{1-\gamma-D_1+D_1^2}{1-R}, \qquad D_3 = 1 - D_1 + D_2,$$

$$Q = \frac{1.25(\gamma - D_3 - D_2)}{D_1}, \qquad R = \frac{\gamma - x_m - D_1^2}{1-\gamma-D_1+D_1^2}.$$

3.2. Application to a plate with reduced section. Validation by experimental tests

In this section, the isogeometric and finite element analyses are performed on a steel specimen. The mechanical properties of the material are given in Table 2. The specimen geometry is depicted in Fig. 6. The reduced section is used to localize the stresses away from the clamp. The bottom side of the plate is fixed while the top side is kept free. The plate is then subjected to a random base acceleration excitation applied to the clamp. To assess the life duration, Dirlik's approach is employed in IGA and FEA. The same excitation was considered in experimental tests to validate the numerical results.

Table 2. Material properties.

Mass density	Young's modulus	Poisson's ratio
7850 kg/m^3	1.7×10^{11} Pa	0.3

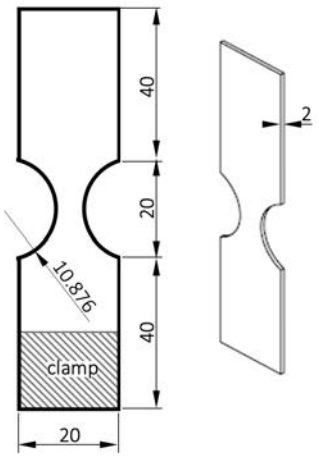

Fig. 6. The plate model with reduced section.

3.3. Numerical analysis

3.3.1. Analysis procedures. As shown in Fig. 7, the static convergence analysis is performed first to obtain an asymptotic stress result. Here, a normal pressure load is applied (in the z-direction, see Fig. 8) onto the free edge of the plate to simulate the bending effect. In the second step, the mesh model resulting from the previous convergence analysis is used to perform the damage calculation for a plate submitted to random loading. The numerical fatigue results are then validated with experimental tests.

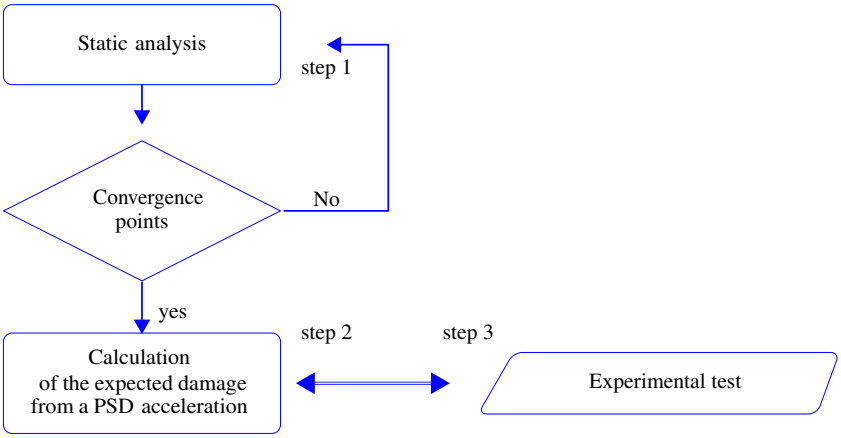

FIG. 7. Flow chart of analysis procedure.

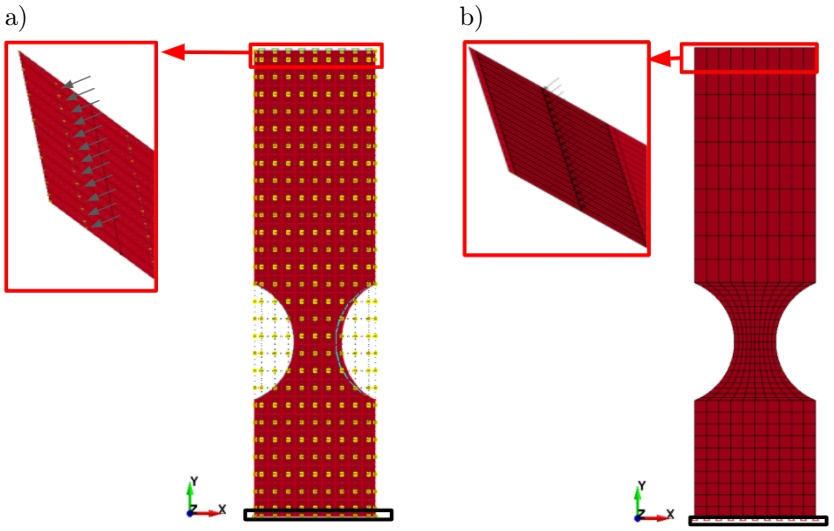

FIG. 8. Mesh models and boundary conditions: a) IGA, b) FEA.

3.3.2. IGA and FEA modelling of the plate. The isogeometric and finite element mesh models are presented in Fig. 8. The boundary conditions are considered similar for IGA and FEA. The clamp is represented by a black box in Fig. 8. The pressure load is fixed at 100 Pa and represented by the red box, is applied to the first top row elements of the model in the minus z-direction to simulate the bending effects in which the applied load area is always 5×20 mm related to the length portion and width of the plate. For IGA, the load is applied onto each NURBS element with a keyword LOAD NURBS Shell in LS-DYNA.

The effective stress results are used for the convergence analyses. From these analyses, presented in Fig. 9, the number of control points for IGA is chosen at 52 and the number of elements for FEA at 133.

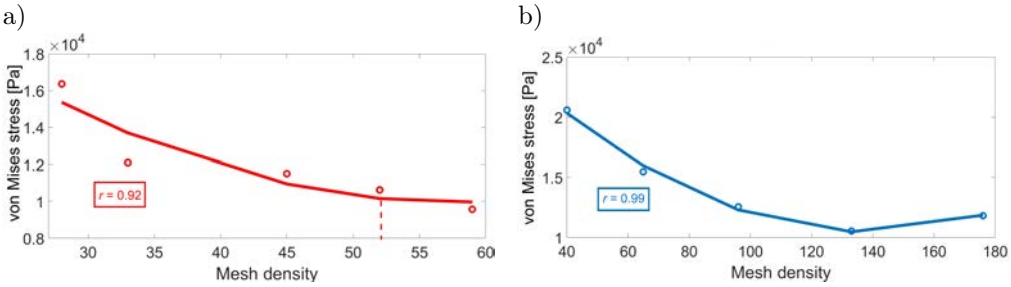

FIG. 9. Convergence results and the related correlation coefficient r of the fitting curves for: a) IGA, b) FEA.

Figure 10 shows the isogeometric and finite element convergence analyses leading to similar maximum stress values (respectively 1.062×10^4 and 1.054×10^4 Pa) with a relative error of 0.75%. Moreover, these maxima are at similar locations of the reduced section. The CPU time of analysis, respectively 231 s and 462 s, shows that IGA is more time-efficient than FEA.

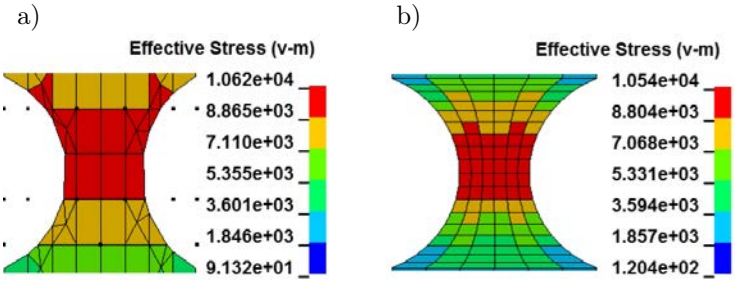

FIG. 10. Effective stress: a) IGA, b) FEA.

3.3.3. Fatigue analysis using power spectral density and damage ratio. After choosing convergence points, the isogeometric and finite element random vibration fatigue analyses are performed on the obtained mesh models. Table 3 and

TABLE 3. The first five natural frequencies [Hz].

	1	2	3	4	5
IGA	211	1282	1510	1623	4253
FEA	209	1141	1506	1579	4266
Relative error [%]	0.9	12.4	0.3	2.8	−0.3

Fig. 11 respectively show the first five natural frequencies and the first vibration mode. Through comparison, it is found that the natural frequencies and vibration mode computed from IGA and FEA are similar. According to Eq. (24), the relative error for the first natural frequency is 0.9%. We can also observe higher relative error for the second and fourth natural frequencies. In our opinion, the difference is due to the low correlation observed in Fig. 9a. Therefore, the number of control points chosen for IGA leads to a small deviation of the von Mises stress in static (see Fig. 10) and to a more consequent deviation in dynamic especially for the pair modes (e.g., torsion). However, only the first mode is useful for this study because it causes the most damage. For this mode, the deviation of the displacements given in Fig. 11 is small.

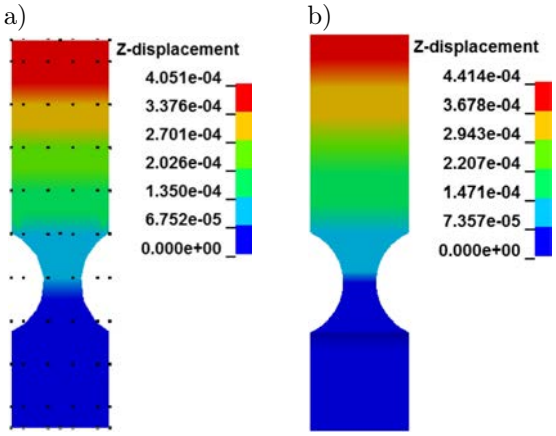

Fig. 11. The first vibration mode: a) IGA, b) FEA.

After the modal analysis, the random analysis is performed with LS-DYNA. The acceleration PSD depicted in Fig. 12 is used to excite the specimen. This PSD is applied on the element nodes (control points for IGA) selected in boundary conditions in the z-direction to simulate the base acceleration. The damping ratio and exposure time are respectively set to 0.016 and 18000 s. The random vibration fatigue analysis is developed in LS-DYNA to obtain the effective stress PSD, the related RMS, and the expected damage. The material constants σ_f and

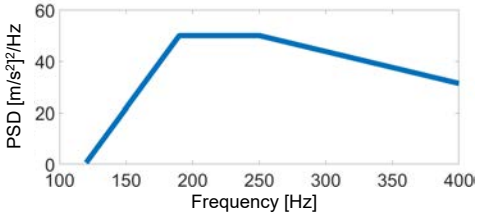

Fig. 12. Applied acceleration PSD.

b of the Basquin's equation (see Eq. (29)) are respectively $612.3 \pm 5\%$ MPa and -0.105, which are obtained from CES EduPack^{TM} software. The margin on σ_f is used to take into consideration the material uncertainty and overcome the small number of specimens tested.

Figures 13 and 14 show the obtained isogeometric and finite element effective stress PSDs and RMS. It can be seen that only the first natural frequency is excited by the acceleration PSD, and the resulting PSD and RMS values are similar. The deviation between the isogeometric and finite element PSDs is due to the difference in the first natural frequencies reported in Table 3. The RMS values of the maximum effective stress obtained from IGA and FEA are respectively 5.24×10^7 and 5.278×10^7 Pa, leading to a relative error of -0.7%. In Fig. 15, it can be seen that the resulting expected damage is respectively 1.45 and 1.47, leading to a relative error of 1.2%. The maximum values of the damage are located in similar locations. According to Eq. (37), the expected fatigue lives are reported in Table 4. It can be observed that for different σ_f, the isogeometric and finite element fatigue lives are in good agreement.

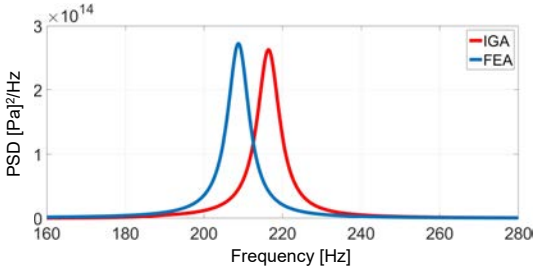

FIG. 13. The effective stress PSD.

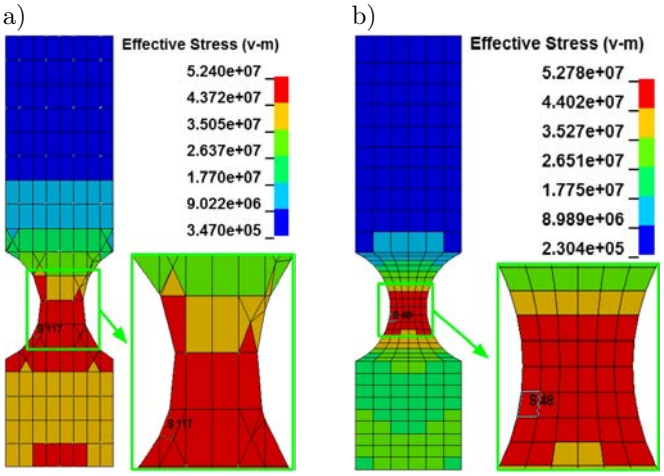

FIG. 14. The effective stress RMS: a) IGA, b) FEA.

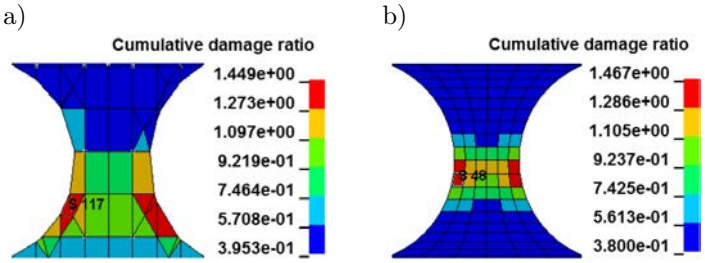

FIG. 15. The cumulative damage ratio: a) IGA, b) FEA.

TABLE 4. Fatigue life results related to the 5% variation of σ_f (in the units of hours : minutes : seconds).

σ_f [MPa]	581.685	612.3	642.915
IGA	2:19:40	3:27:02	4:48:43
FEA	2:17:06	3:24:30	4:46:48

3.4. Experimental test

Three specimens were tested in fatigue induced by vibration. The test was carried out with random acceleration using the electrodynamic shaker TiraVib TV50100 + BAA1000 + 114 FPS (Fig. 16a) from the Mechanical Laboratory of Normandy [41, 42]. Figure 16b gives a schematic representation of the system.

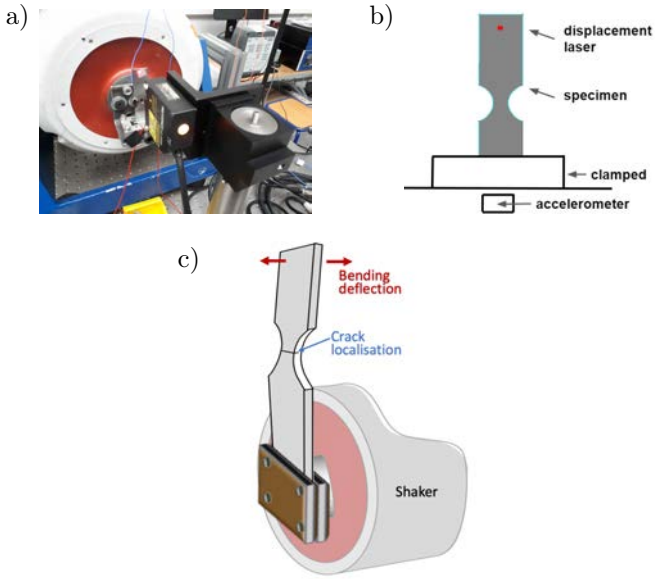

FIG. 16. a) Vibration-based bending fatigue bench, b) scheme of the test, and c) scheme of the bending deflection.

The series of three specimens used for the experimental tests are made up of low-carbon steel DC01 (or St10 or XC10 or SAE 1010) with the yield stress of 235 MPa and Young's modulus of 170 GPa. A reduced section was designed in the specimen to locate the crack away from the clamp. The specimen was clamped on one edge, and the remaining edge was free. A transversal vibration (Fig. 16c) was imposed at the clamp by driving the shaker with a closed-loop control device (ACP or Acquisition Control Peripheral of spectral dynamic "Jaguar"). The shaker drive was possible thanks to an accelerometer PCB 333A30 mounted at the specimen fixture. The response measurements of the specimen were given by a laser displacement sensor located at the free edge and a strain gauge HBM 1LY15-1.5/350 was glued at the centre of the reduced section of the specimen. The input acceleration PSD was identical to that used in the numerical analysis (see Fig. 12). One thousand six hundred frequency lines were used to generate the related time signal. Frequency and time signal responses were continuously recorded by the ACP and an "HBM quantum" device, respectively. The frequency response corresponding to the ratio of the displacement over the input acceleration was used to follow the resonant frequency of the system. If a crack occurs (see Fig. 16c), a shift and a decrease of magnitude of the frequency response are observed. Figure 17 shows the frequency responses recorded at different times of a fatigue test. An amplitude decrease is observed when cumulative damage occurs. Therefore, it is possible to detect a change in the response of the specimen by the evolution of the resonant frequency deviation defined by the following ratio:

$$\text{RFD } [\%] = 100 \times \frac{f_r^0 - f_r^i}{f_r^0}, \tag{41}$$

where f_r^0 corresponds to the initial resonant frequency of undamaged specimen and f_r^i is the i-th measure of the resonant frequency during the fatigue test.

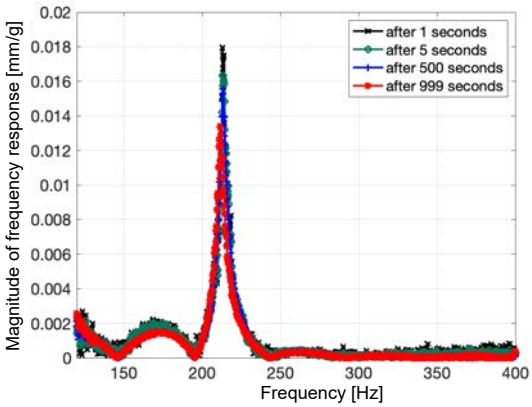

FIG. 17. Frequency responses during fatigue test (four measures).

The strain signal in time recorded by the HBM device via the strain gauge is represented in Fig. 18 for specimen S1 (with a sampling rate of 4800 of per second). The related spectrogram given in Fig. 19 shows the evolution of resonant frequency during the exposure time. The deviation of this resonant frequency is clearly visible.

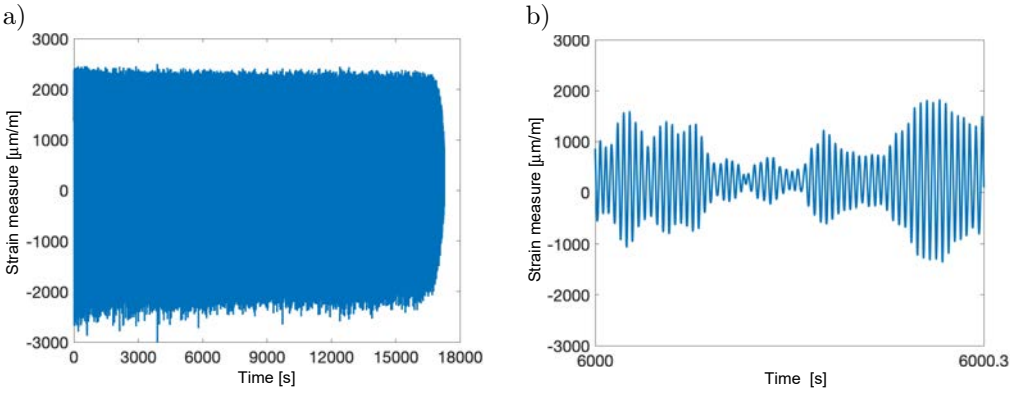

FIG. 18. Strain measure (a) complete signal during fatigue test and (b) signal zoom.

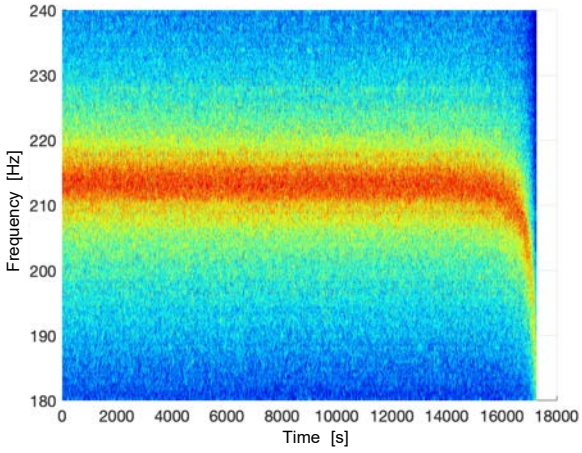

FIG. 19. Spectrogram obtained from the strain measure.

Figure 20 represents the RFD evolution extracted from the spectrogram. This evolution represents the time versus the number of cycles deduced from the frequency. After the occurrence of crack, it can be observed that the RFD values increase with the crack growth. Based on the studies of Xu *et al.* [43] and Hu *et al.* [44], the fatigue lives of the specimens were determined for the RFD threshold fixed at 5%. The resulting fatigue lives obtained after the test

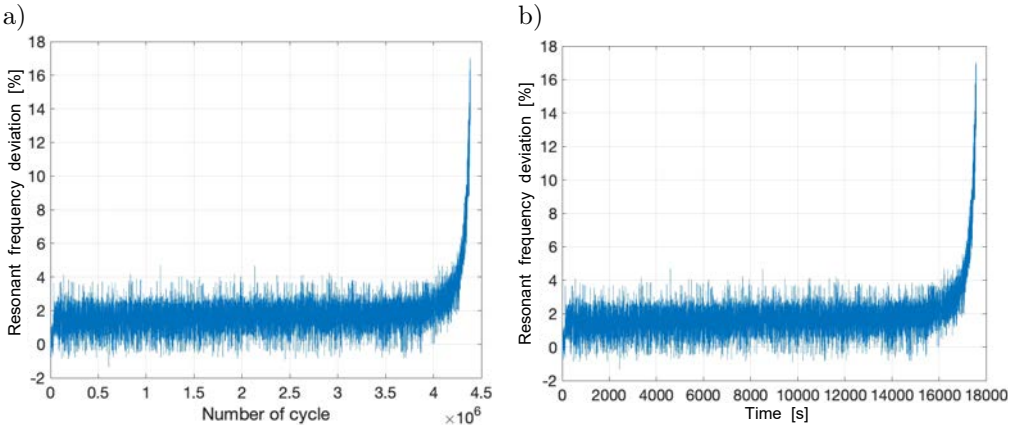

FIG. 20. Resonant frequency deviation during fatigue test (a) *versus* time and (b) *versus* number of cycles.

of the three specimens are reported in Table 5. The lifetimes obtained from the experimental tests are within the range obtained numerically from the values of σ_f.

TABLE 5. The experimental fatigue lives obtained for 5% frequency drop (hour : minutes : seconds).

Id of specimen	Fatigue life
S_1	4:26:40
S_2	3:30
S_3	3:16:45

4. Conclusion

The objective of this study was to propose a new method of numerical modelling for the fatigue life prediction of structures. We considered the random vibration fatigue analysis on a steel plate with a reduced section. The specimen was clamped on one side and random acceleration in the normal direction to the plate surface was applied on the fixture side. IGA was chosen for modelling because it potentially allows for faster numerical simulations, which is important for complex structures. The finite element model was also computed for comparison. We chose the LS-DYNA software for the numerical modelling.

The convergence analysis of the static bending problem was used to define the mesh density. It is shown that the IGA and FEA convergence analyses led to similar maximum stress values with a relative error of 0.75%, and are situated at similar locations of the reduced section. The CPU time of the analysis, re-

spectively 231 and 462 seconds, shows that IGA is more time efficient compared to FEA.

The convergence analysis highlighted that for IGA during each mesh refinement step, there is no need to re-create mesh elements on the original geometry model. It is sufficient to develop mesh elements on the previous mesh model, so that the mesh refinement time can be greatly saved. However, for FEA, it is mandatory to communicate with the original geometric model for mesh refinement, and so this process is more time-consuming in LS-DYNA software.

The comparison of numerical analysis results, shows that the effective stress power spectral densities and the related root mean square values are similar, with a relative error of -0.7%. This small inaccuracy is probably due to the convergence and the choice of the number of finite elements and control points. Despite this, IGA can predict the fatigue life using fewer NURBS elements and integration points through the thickness, and the predictions are consistent with the FEA result.

These results were estimated by experimental tests. In fact, the experimentally obtained lifetimes are effectively evaluated by IGA and FEA, leading to the conclusion that these analyses are suitable for random vibration fatigue.

Acknowledgements

The authors gratefully acknowledge the support from the China Scholarship Council (CSC).

Declaration of Interest Statement

The authors declare that they have no known competing financial interests or personal relationships that could influence the work reported in this paper.

Highlights

- A numerical model is implemented in LS-DYNA to predict the fatigue damage of a specimen under random vibrations in the frequency domain.
- Isogeometric analysis is used for the numerical modelling.
- Finite element models are used for the comparison.
- Convergence rates are compared, and IGA models converge with less mesh density.
- Isogeometric random vibration fatigue analysis can predict similar results with finite element counterparts (with a relative error of 1.2% for the cumulative damage).

- The analysis results are validated by experimental test, concluding that the isogeometric analysis is appropriate for random vibration fatigue problems.

References

1. A. Ringeval, Y. Huang, Random vibration fatigue analysis with LS-DYNA, [in:] *Proceedings of the 12th International LS-DYNA Users Conference*, Dearborn, Michigan, USA, 2012.

2. T. Dirlik, *Application of computers in fatigue analysis*, PhD thesis, University of Warwick, Coventry, England, 1985.

3. S.J. Owen *et al.*, An immersive topology environment for meshing, [in:] M.L. Brewer, D. Marcum [Eds], *Proceedings of the 16th International Meshing Roundtable*, pp. 553–577, Springer, Berlin, Heidelberg, 2008.

4. T.J.R. Hughes, J.A. Cottrell, Y. Bazilevs, Isogeometric analysis: CAD, finite elements, NURBS, exact geometry and mesh refinement, *Computer Methods in Applied Mechanics and Engineering*, **194**(39): 4135–4195, 2005, doi: 10.1016/j.cma.2004.10.008.

5. J. Lu, Isogeometric contact analysis: Geometric basis and formulation for frictionless contact, *Computer Methods in Applied Mechanics and Engineering*, **200**(5–8): 726–741, 2011, doi: 10.1016/j.cma.2010.10.001.

6. İ. Temizer, P. Wriggers, T.J.R. Hughes, Contact treatment in isogeometric analysis with NURBS, *Computer Methods in Applied Mechanics and Engineering*, **200**(9–12): 1100–1112, 2011, doi: 10.1016/j.cma.2010.11.020.

7. İ. Temizer, P. Wriggers, T.J.R. Hughes, Three-dimensional mortar-based frictional contact treatment in isogeometric analysis with NURBS, *Computer Methods in Applied Mechanics and Engineering*, **209–212**: 115–128, 2012, doi: 10.1016/j.cma.2011.10.014.

8. Y. Bazilevs, T.J.R. Hughes, NURBS-based isogeometric analysis for the computation of flows about rotating components, *Computational Mechanics*, **43**: 143–150, 2008, doi: 10.1007/s00466-008-0277-z.

9. Y. Bazilevs, V.M. Calo, Y. Zhang, T.J.R. Hughes, Isogeometric fluid–structure interaction analysis with applications to arterial blood flow, *Computational Mechanics*, **38**: 310–322, 2006, doi: 10.1007/s00466-006-0084-3.

10. Y. Bazilevs, V.M. Calo, T.J.R. Hughes, Y.J. Zhang, Isogeometric fluid-structure interaction: theory, algorithms, and computations, *Computational Mechanics*, **43**: 3–37, 2008, doi: 10.1007/s00466-008-0315-x.

11. X. Qian, Full analytical sensitivities in NURBS based isogeometric shape optimization, *Computer Methods in Applied Mechanics and Engineering*, **199**(29–32): 2059–2071, 2010, doi: 10.1016/j.cma.2010.03.005.

12. W.A. Wall, M.A. Frenzel, C. Cyron, Isogeometric structural shape optimization, *Computer Methods in Applied Mechanics and Engineering*, **197**(33–40): 2976–2988, 2008, doi: 10.1016/j.cma.2008.01.025.

13. B. Hassani, S.M. Tavakkoli, N.Z. Moghadam, Application of isogeometric analysis in structural shape optimization, *Scientia Iranica*, **18**(4): 846–852, 2011, doi: 10.1016/j.scient.2011.07.014.

14. S. Shojaee, N. Valizadeh, M. Arjomand, Isogeometric structural shape optimization using particle swarm algorithm, *International Journal of Optimization in Civil Engineering*, **1**(4): 633–645, 2011.

15. J. Kiendl, K.-U. Bletzinger, J. Linhard, R. Wüchner, Isogeometric shell analysis with Kirchhoff–Love elements, *Computer Methods in Applied Mechanics and Engineering*, **198**(49–52): 3902–3914, 2009, doi: 10.1016/j.cma.2009.08.013.

16. D.J. Benson, Y. Bazilevs, M.-C. Hsu, T.J.R. Hughes, Isogeometric shell analysis: The Reissner-Mindlin shell, *Computer Methods in Applied Mechanics and Engineering*, **199**(5–8): 276–289, 2010, doi: 10.1016/j.cma.2009.05.011.

17. D.J. Benson, Y. Bazilevs, M.-C. Hsu, T.J.R. Hughes, A large deformation, rotation-free, isogeometric shell, *Computer Methods in Applied Mechanics and Engineering*, **200**(13–16): 1367–1378, 2011, doi: 10.1016/j.cma.2010.12.003.

18. T.-K. Uhm, S.-K. Youn, T-spline finite element method for the analysis of shell structures, *International Journal for Numerical Methods in Engineering*, **80**: 507–536, 2009, doi: 10.1002/nme.2648.

19. J. Kiendl, Y. Bazilevs, M.-C. Hsu, R. Wüchner, K.-U. Bletzinger, The bending strip method for isogeometric analysis of Kirchhoff–Love shell structures comprised of multiple patches, *Computer Methods in Applied Mechanics and Engineering*, **199**(37–40): 2403–2416, 2010, doi: 10.1016/j.cma.2010.03.029.

20. S.-I. Moon, I.-J. Cho, D. Yoon, Fatigue life evaluation of mechanical components using vibration fatigue analysis technique, *Journal of Mechanical Science and Technology*, **25**: 631–637, 2011, doi: 10.1007/s12206-011-0124-6.

21. Y. Eldoğan, E. Ciğeroğlu, Vibration fatigue analysis of a cantilever beam using different fatigue theories, [in:] R. Allemang, J. De Clerck, C. Niezrecki, A. Wicks [Eds], *Topics in Modal Analysis*, Vol. 7, Conference Proceedings of the Society for Experimental Mechanics Series, pp. 471–478, Springer, New York, NY, 2014, doi: 10.1007/978-1-4614-6585-0_45.

22. J.A. Cottrell, A. Reali, Y. Bazilevs, T.J.R. Hughes, Isogeometric analysis of structural vibrations, *Computer Methods in Applied Mechanics and Engineering*, **195**(41–43): 5257–5296, 2006, doi: 10.1016/j.cma.2005.09.027.

23. D. Wang, W. Liu, H. Zhang, Novel higher order mass matrices for isogeometric structural vibration analysis, *Computer Methods in Applied Mechanics and Engineering*, **260**: 92–108, 2013, doi: 10.1016/j.cma.2013.03.011.

24. S. Shojaee, E. Izadpanah, N. Valizadeh, J. Kiendl, Free vibration analysis of thin plates by using a NURBS-based isogeometric approach, *Finite Elements in Analysis and Design*, **61**: 23–34, 2012, doi: 10.1016/j.finel.2012.06.005.

25. S. Gondegaon, H.K. Voruganti, Static structural and modal analysis using isogeometric analysis, *Journal of Theoretical and Applied Mechanics*, **46**(4): 36–75, 2016, doi: 10.1515/jtam-2016-0020.

26. T.D. Hien, H.-C. Noh, Stochastic isogeometric analysis of free vibration of functionally graded plates considering material randomness, *Computer Methods in Applied Mechanics and Engineering*, **318**: 845–863, 2017, doi: 10.1016/j.cma.2017.02.007.

27. S. Hartmann, D.J. Benson, D. Lorenz, About isogeometric analysis and the new NURBS-based finite elements in LS-DYNA, [in:] *8th European LS-DYNA Users Conference*, Strasbourg, France, 2011.

28. Y. Huang, S. Hartmann, D.J. Benson, Random vibration fatigue analysis based on IGA model in LS-DYNA, *Ansys TechCon 2020*, October 2020, https://ftp.lstc.com/anonymous/outgoing/huang/nvh/papers.htm.

29. V. Agrawal, S.S. Gautam, IGA: A simplified introduction and implementation details for finite element users, *Journal of The Institution of Engineers (India): Series C*, **100**: 561–585, 2019, doi: 10.1007/s40032-018-0462-6.

30. O.C. Zienkiewicz, R.L. Taylor, J.Z. Zhu, *The Finite Element Method: Its Basis and Fundamentals*, 6th Ed., Elsevier, Butterworth-Heinemann, 2005.

31. P. Milić, D. Marinković, Isogeometric structural analysis based on NURBS shape functions, *Facta Universitatis, Series: Mechanical Engineering*, **11**(2): 193–202, 2013.

32. G. Kirsch, Die Theorie der Elastizität und die Bedurfnisse der Festigkeitslehre [in German], *Zantralblatt Verlin Deutscher Ingenieure*, **42**: 797–807, 1898.

33. J. Schijve, Four lectures on fatigue crack growth: I. Fatigue crack growth and fracture mechanics, *Engineering Fracture Mechanics*, **11**: 169–181, 1979.

34. M.A. Miner, Cumulative damage in fatigue, *Journal of Applied Mechanics*, **12**(3): 159–164, 1945, doi: 10.1115/1.4009458.

35. A. Palmgren, Die Lebensdauer von Kugellagern [in German; in English: Durability of ball bearings], *Zeitschrift des Vereines Deutscher Ingenieure (ZVDI)*, **14**: 339–341, 1924.

36. B.R. Krasnowski, *Application of damage tolerance to increase safety of helicopters in service*, Defense Technical Information Center, 1999.

37. A. Strauss, D.M. Frangopol, K. Bergmeister, Life-cycle and Sustainability of Civil Infrastructure Systems, [in:] A. Strauss, D. M. Frangopol, K. Bergmeister [Eds], *Proceedings of the Third International Symposium on Life-Cycle Civil Engineering*, Vienna, Austria, October 3–6, 2012, CRC Press, 2013.

38. G. Risitano, D. Corallo, A. Risitano, Cumulative damage by Miner's rule and by energetic analysis, *Structural Durability Health Monitoring*, **8**(2): 91–109, 2012, doi: 10.3970/sdhm.2012.008.091.

39. Y.-L. Lee, D. Taylor, Cycle counting techniques, [in:] Y.-L. Lee, J. Pan, R.B. Hathaway, M.E. Barkey [Eds], *Fatigue Testing and Analysis*, vol. 3, pp. 77–102, Burlington, Butterworth-Heinemann, 2005.

40. I. Milne, R.O. Ritchie, B.L. Karihaloo, Cyclic loading and fatigue, [in:] R.O. Ritchie, Y. Murakami [Eds], *Comprehensive Structural Integrity. Volume 4: Cyclic Loading and Fatigue*, Elsevier, 2003.

41. A. Appert, C. Gautrelet, L. Khalij, R. Troian, Development of a test bench for vibratory fatigue experiments of a cantilever beam with an electrodynamic shaker, [in:] *Proceedings*

of the 12th International Fatigue Congress (FATIGUE 2018). MATEC Web Conferece, vol. 165, 8 pages, 2018, doi: 10.1051/matecconf/201816510007.

42. L. Khalij, C. Gautrelet, A. Guillet, Fatigue curves of a low carbon steel obtained from vibration experiments with an electrodynamic shaker, *Materials and Design*, **86**: 640–648, 2015, doi: 10.1016/j.matdes.2015.07.153.

43. W. Xu, X. Yang, B. Zhong, Y. He, C. Tao, Failure criterion of titanium alloy irregular sheet specimens for vibration-based bending fatigue testing, *Engineering Fracture Mechanics*, **195**: 44–56, 2018, doi: 10.1016/j.engfracmech.2018.03.031.

44. H.-T. Hu, Y.-L. Li, T. Suo, F. Zhao, Y.-G. Miao, P. Xue, Q. Deng, Fatigue behavior of aluminum stiffened plate subjected to random vibration loading, *Transactions of Nonferrous Metals Society of China*, **24**(5): 1331–1336, 2014, doi: 10.1016/S1003-6326(14)63196-4.

Received June 28, 2021; revised version January 13, 2022.